

**Three-body correlations in direct reactions: Example of  ${}^6\text{Be}$  populated in the  $(p, n)$  reaction**

V. Chudoba,<sup>1,2,\*</sup> L. V. Grigorenko,<sup>1,3,4</sup> A. S. Fomichev,<sup>1,5</sup> A. A. Bezbakh,<sup>1,2</sup> I. A. Egorova,<sup>6,7</sup> S. N. Ershov,<sup>6</sup> M. S. Golovkov,<sup>1,5</sup> A. V. Gorshkov,<sup>1</sup> V. A. Gorshkov,<sup>1</sup> G. Kaminski,<sup>1,8</sup> S. A. Krupko,<sup>1</sup> I. Mukha,<sup>9</sup> E. Yu. Nikolskii,<sup>1,4</sup> Yu. L. Parfenova,<sup>1</sup> S. I. Sidorchuk,<sup>1</sup> P. G. Sharov,<sup>1,2</sup> R. S. Slepnev,<sup>1</sup> L. Standlyo,<sup>10</sup> S. V. Stepantsov,<sup>1</sup> G. M. Ter-Akopian,<sup>1,5</sup> R. Wolski,<sup>1,11</sup> and M. V. Zhukov<sup>12</sup>

<sup>1</sup>*Flerov Laboratory of Nuclear Reactions, JINR, 141980 Dubna, Russia*

<sup>2</sup>*Institute of Physics, Silesian University in Opava, 74601 Opava, Czech Republic*

<sup>3</sup>*National Research Nuclear University “MEPhI”, 115409 Moscow, Russia*

<sup>4</sup>*National Research Centre “Kurchatov Institute”, Kurchatov sq. 1, 123182 Moscow, Russia*

<sup>5</sup>*State University Dubna, 141980 Dubna, Russia*

<sup>6</sup>*Bogoliubov Laboratory of Theoretical Physics, JINR, 141980 Dubna, Russia*

<sup>7</sup>*Department of Physics, Western Michigan University, Kalamazoo, Michigan 49008, USA*

<sup>8</sup>*Heavy Ion Laboratory, University of Warsaw, 02-093 Warsaw, Poland*

<sup>9</sup>*GSI Helmholtzzentrum für Schwerionenforschung, 64291 Darmstadt, Germany*

<sup>10</sup>*Heavy Ion Laboratory, University of Warsaw, Pasteura 5A, Warsaw, Poland*

<sup>11</sup>*Institute of Nuclear Physics PAN, Radzikowskiego 152, 31342 Kraków, Poland*

<sup>12</sup>*Department of Physics, Chalmers University of Technology, S-41296 Göteborg, Sweden*



(Received 13 February 2018; revised manuscript received 6 June 2018; published 21 November 2018)

The  ${}^6\text{Be}$  continuum states were populated in the charge-exchange reaction  ${}^1\text{H}({}^6\text{Li}, {}^6\text{Be})n$  collecting very high statistics data ( $\sim 5 \times 10^6$  events) on the three-body  $\alpha + p + p$  correlations. The  ${}^6\text{Be}$  excitation energy region below  $\sim 3$  MeV is considered, where the data are dominated by contributions from the  $0^+$  and  $2^+$  states. It is demonstrated how the high-statistics few-body correlation data can be used to extract detailed information on the reaction mechanism. Such a derivation is based on the fact that highly spin-aligned states are typically populated in the direct reactions.

DOI: [10.1103/PhysRevC.98.054612](https://doi.org/10.1103/PhysRevC.98.054612)

**I. INTRODUCTION**

The nuclear driplines are defined by instability with respect to particle emission, and therefore the entire spectra of the systems beyond the driplines are continuous. The first emission threshold in the light even systems is often, due to pairing interaction, the threshold for two-neutron or two-proton emission, and therefore one has to deal with three-body continuum. In certain systems, just beyond the dripline, the continuum of more fragments in the final state can be encountered (e.g.,  ${}^7\text{H}$ ,  ${}^8\text{C}$ ,  ${}^{28}\text{O}$ ), so we should speak about few-body continuum. Few-body continuum provides rich information about nuclear structure of ground-state and continuum excitations, which is, however, often tightly intertwined with contributions of reaction mechanism. The way to extract this information is to explore the world of various correlations in fragment motions and to look for methods to disentangle contributions of reaction mechanisms.

Nuclear reactions provide much broader opportunities to study correlations in comparison with nuclear decays. Any reaction has at least one selected direction—the direction of a projectile momentum—and correlations of the reaction products relative to this direction can be studied. This fact is

the starting point for a widespread method of spin-parity ( $J^\pi$ ) identification in the excitation spectrum: experimental angular distribution of the reaction products is compared to Born-type calculations. Such angular distributions can be qualitatively described in terms of transferred momentum  $\mathbf{q}$  and transferred angular momentum  $\Delta L$  by a simple analytical expression for differential cross section

$$\frac{d\sigma_{\Delta L}}{d\Omega} \sim |j_{\Delta L}(qr_0)|^2, \quad (1)$$

where  $j_{\Delta L}$  is spherical Bessel function and  $r_0$  is some typical size of the reaction volume. In spite of quite qualitative character of the dependence Eq. (1), in some cases, it could be sufficient for complete  $J^\pi$  identification. Applications of such methods are limited by field of direct reactions, where the Born-type approximations are robust.

Alternative method of spin-parity identification can be used for a narrower class of the direct reactions populating states in the continuum. Namely, for direct reactions, which can be well described by the pole mechanism [or single diagram with transfer of one species, see Fig. 1(a)], where one-step reaction gives dominating contribution. Such a mechanism is widespread at intermediate (20–70 A MeV) and high ( $>70$  A MeV) energies, which are commonly used in the modern radioactive ion beam (RIB) research. It selects one exceptional direction in space defined by the vector of

\*chudoba@jinr.ru

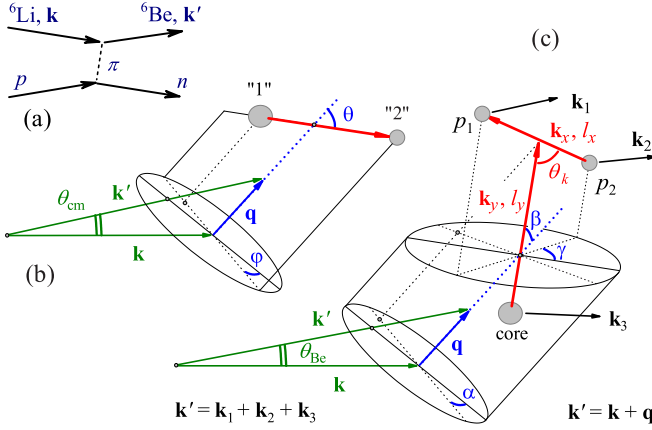


FIG. 1. Schematic presentation of  ${}^6\text{Be}$  population in charge-exchange reaction and correlations available for particle-unstable states. (a) Single-pole reaction mechanism. Complete kinematics description for correlations following the (b) two-body and (c) three-body decays. In (c), the center-of-mass angle  $\theta_{\text{Be}}$  (green color) describe scattering of  ${}^6\text{Be}$  as a whole, red color shows kinematical variables associated with internal correlations, while blue ones are responsible for external correlations describing orientation of system as a whole.

the transferred momentum  $\mathbf{q}$ . In the coordinate frame where  $Z$  axis is parallel to  $\mathbf{q}$ , only a zero projection  $\Delta M = 0$  of the orbital angular momentum  $\Delta L$  can be transferred.

$$\{[\Delta \mathbf{L} \times \mathbf{q}] \equiv 0, Z \parallel \mathbf{q}\} \rightarrow \Delta M = 0. \quad (2)$$

This simple result is obtained only in the case of spinless particles transfer. In this case, for example, from initial state with  $J_i = 0$ , the final state with magnetic quantum number  $M_f = 0$  only may be populated for whichever  $J_f$ . This is one of extreme situations of spin alignment, characterized as polar alignment. A situation with nonzero spin transfer alignment should be more complicated. However, in many reaction scenarios the states with  $J_f > 1/2$  are populated with high spin alignment in the momentum transfer frame even in the case of nonzero spin transfer. For highly aligned states, decaying via particle emission, the angular distributions with respect to the momentum transfer axis  $Z \parallel \mathbf{q}$  could have very distinctive shape, which can be used for spin-parity identification.

For continuum states of neutron-rich systems and for proton-rich systems above the Coulomb barrier the situation of broad overlapping states is quite common. Interference of broad overlapping states in continuum may further enhance correlation patterns and add features facilitating spin-parity identification. For example, for the pole transfer mechanism the correlation patterns for an isolated resonance observed in the momentum transfer frame should be symmetric with respect to  $\pi/2$  polar angle. However, in the case of interference of states with opposite parities an asymmetric correlation patterns may arise. Thus, spin alignment induced by reaction mechanism and interference of broad overlapping states in continuum are the major physical phenomena defining the proposed method.

This method was often used for spin-parity identification of excited states decaying via emission of (mainly spinless) particles in the past ([1] and references therein). During the last decade, such an approach was applied to exotic neutron- and proton-rich systems beyond the driplines in the experiments at the Flerov Laboratory of Nuclear Reactions at JINR (Dubna, Russia). For example, the interference patterns for broad overlapping states with different  $J^\pi$  were used for unambiguous spin-parity identification of low-lying  ${}^9\text{He}$  continuous states decaying via  ${}^8\text{He} + n$  channel [2]. An analogous method can be used for three-body systems, however in a technically much more complicated manner. The examples of such a  $J^\pi$  identification in three-body systems can be found for  ${}^5\text{H}$  [3,4] and for  ${}^{10}\text{He}$  states [5].

The first results of the experiment studying the  $\alpha + p + p$  correlations in decays of the  ${}^6\text{Be}$  states populated in the  $(p, n)$  charge-exchange reaction were published in Ref. [6]. The paper was focused on the proof that the observed  ${}^6\text{Be}$  excitation spectrum above  $\sim 3$  MeV is dominated by the novel phenomenon—isovector breed of the soft dipole mode built on the  ${}^6\text{Li}$  ground state (g.s.). In this work we consider the correlations in the decay of  ${}^6\text{Be}$  states with excitation energy below  $\sim 3$  MeV, where the data are dominated by the contributions of the known and well-understood  $0^+$  and  $2^+$  states of  ${}^6\text{Be}$ . We pursue a sort of an opposite aim to Refs. [2–5]. We demonstrate that basing on the known level scheme it is possible to extract from the three-body correlations the maximal possible quantum mechanical information about reaction mechanism (e.g., the density-matrix parameters) thus paving the way to its in-depth theoretical studies.

Unit system  $\hbar = c = 1$  is used in this work. The paper is structured in the following way. First, kinematics notations are given for three-particle correlations detected in a reaction with four particles in final state (Sec. II). Then a description of the applied theoretical model is presented in Sec. III in detail. The experimental setup and conditions are given in Sec. IV. The data analysis is described in Sec. V, and the physics discussion and conclusions are in Secs. VI and VII, respectively.

## II. THREE-BODY CORRELATIONS

Let us consider three-body correlations obtained in the nuclear reaction  ${}^6\text{Li} + p \rightarrow (p + p + \alpha) + n$ . In general, the spin-averaged cross section for a collision  $A + p \rightarrow k_1 + k_2 + k_3 + k_n$  of a projectile  $A$  and a proton target  $p$ , leading to the four fragments in the final state, can be written in the following way:

$$\sigma = \frac{(2\pi)^4}{v_i} \frac{1}{j_A^2 j_p^2} \sum \int d\mathbf{k}_1 d\mathbf{k}_2 d\mathbf{k}_3 d\mathbf{k}_n \times \delta(E_f - E_i) \delta(\mathbf{P}_f - \mathbf{P}_i) |T_{fi}|^2, \quad (3)$$

where  $E_i = E_p + E_A$ ,  $E_f = E_1 + E_2 + E_3 + E_n + Q$ ,  $\mathbf{P}_i = \mathbf{k}_p + \mathbf{k}_A$ ,  $\mathbf{P}_f = \mathbf{k}_1 + \mathbf{k}_2 + \mathbf{k}_3 + \mathbf{k}_n$  are the total energies and momenta of all particles before and after collisions, respectively.  $Q = -3.70$  MeV is the reaction  $Q$  value calculated in respect to the three-body threshold in the final state,  $E_j$  is a kinetic energy of particle  $j$ . The relative incident velocity and

the reduced mass of the nuclei before collision are

$$v_i = \frac{k_i}{\mu_i}, \quad \mu_i = \frac{m_p m_A}{m_p + m_A}.$$

Shortcut  $\hat{J} = \sqrt{2J+1}$  is used in (3), and the summation is over spin projections of all particles before and after collision. In the  $(p+A)$  center-of-mass (c.m.) coordinate frame  $\mathbf{P}_i = 0$ ,  $\mathbf{k}_A = -\mathbf{k}_p = \mathbf{k}$ ,  $E_i = k^2/2\mu_i$ . Our prime interest is in studies of nuclear systems consisting of the three particles  $k_1$ ,  $k_2$ , and  $k_3$ . Then, the fragment relative motion in three-body continuum can be described by two relative Jacobi momenta  $\mathbf{k}_x$  and  $\mathbf{k}_y$  and the c.m. momentum  $\mathbf{k}'$  of the three particles

$$\begin{aligned} \mathbf{k}_x &= \mu_x \left( \frac{\mathbf{k}_1}{m_1} - \frac{\mathbf{k}_2}{m_2} \right), & \mu_x &= \frac{m_1 m_2}{m_1 + m_2} \\ \mathbf{k}_y &= \mu_y \left( \frac{\mathbf{k}_1 + \mathbf{k}_2}{m_1 + m_2} - \frac{\mathbf{k}_3}{m_3} \right), & \mu_y &= \frac{(m_1 + m_2)m_3}{m_1 + m_2 + m_3} \\ \mathbf{P}_f &= 0, & \mathbf{k}' &= \mathbf{k}_1 + \mathbf{k}_2 + \mathbf{k}_3 = -\mathbf{k}_4. \end{aligned} \quad (4)$$

For each three-body decay event, the Jacobi momenta  $\mathbf{k}_x$  and  $\mathbf{k}_y$  define the decay plane. The internal correlations of the fragments [shown by red color in Fig. 1(c)] are defined within this plane while external correlations [blue colored in Fig. 1(c)] defines orientation of this plane with respect to the reaction plane [green colored in Fig. 1(c)], which is fixed by the initial  $\mathbf{k}$  and final  $\mathbf{k}'$  c.m. momenta.

Internal three-body correlations for the Jacobi momenta  $\mathbf{k}_x$  and  $\mathbf{k}_y$  are conveniently described by two parameters  $\{\varepsilon, \theta_k\}$  in the following way:

$$\begin{aligned} \varepsilon &= E_x/E_T, & \cos(\theta_k) &= (\hat{\mathbf{k}}_x \cdot \hat{\mathbf{k}}_y) \\ E_T &= E_x + E_y = k_x^2/2\mu_x + k_y^2/2\mu_y. \end{aligned} \quad (5)$$

The three-body decay energy  $E_T$  fixes only a total phase volume accessible for the three fragments, and the fragment kinetic energies have continuous distributions within this volume. In addition, two relative orbital angular momenta  $l_x$  and  $l_y$ , corresponding to the  $\mathbf{k}_x$  and  $\mathbf{k}_y$  momenta, characterize their motion. Since in the  ${}^6\text{Be}$  two fragments are identical protons, only two different distinguishable Jacobi coordinate systems exist. One, labeled ‘‘T’’, corresponds to the case when particles 1 and 2 are protons with relative momentum  $\mathbf{k}_x$ , while particle 3 is the  $\alpha$  particle. In the second case, called ‘‘Y’’, the relative momentum  $\mathbf{k}_x$  is defined by the proton with index 1 and  $\alpha$  particle with index 2, while the other proton has index 3. The variables  $\{\varepsilon, \theta_k\}$  depend on the Jacobi systems while the energy  $E_T$  is invariant, i.e., independent from this choice. The representations ‘‘T’’ and ‘‘Y’’ are equivalent. In spite of this, we use both systems, since certain aspects of correlation can be better revealed in one of them. For example, in the ‘‘T’’ system the parameter  $\varepsilon$  describes the energy correlation between two protons, while in the ‘‘Y’’ it is connected with core- $p$  energy correlations in  ${}^6\text{Be}$ . It is convenient to distinguish parameters  $\{\varepsilon_T, \theta_k^{(T)}\}$  and  $\{\varepsilon_Y, \theta_k^{(Y)}\}$  in Jacobi ‘‘T’’ and ‘‘Y’’ systems, respectively.

External correlations describe the orientation of the three-body decay plane relative to the selected direction. We choose this direction along the transferred momentum  $\mathbf{q} = \mathbf{k}' - \mathbf{k}$

lying in the reaction plane. In this case the external correlations are three Euler angles labeled as  $\{\alpha, \beta, \gamma\}$  in Fig. 1(c). This choice has an advantage over other possibilities in the case of one-step reaction mechanism domination. In such a case the particle transfer can be described in a single-pole approximation and there should be rotational invariance with respect to vector  $\mathbf{q}$ . The decay dynamics will be independent from the angle  $\alpha$ . This is a manifestation of the so-called Treiman-Yang criterion for the dominance of a single-pole mechanism of direct reactions [7,8]. This criterion is an important and useful tool to check the assumption on a reaction mechanism providing its necessary condition, and the experimental data can be tested on agreement to it. Concerning other external parameters, the dependence on the orientation angle  $\beta$  for three-body decays is easy to interpret, as will be shown below, while an interpretation of the  $\gamma$  parameter is not straightforward.

In the end of this section we briefly summarize differences between two- and three-body correlations observed in the decays and in the reactions. On the one hand, the orientation of the system as a whole is assumed to be isotropic in decays, as far as the system has forgotten how it was populated. On the other hand, reactions may have several selected directions in the space. The one is the beam direction. For direct reactions with single-pole mechanism there is, as mentioned above, another important direction: the transferred momentum  $\mathbf{q}$ . So, two following features for the decays and reactions with subsequent two-body and three-body decay can be emphasized:

(i) Two-body decay is characterized just by two parameters: energy and width of the state. In contrast, for description of three-body decays, except the energy and width of the state, we need additional parameters, so-called internal correlation parameters  $\varepsilon$  and  $\cos(\theta_k)$ .

(ii) Population of spin-aligned states is common for nuclear reactions. Two additional parameters related to orientation  $\{\theta, \varphi\}$  are needed to describe the two-body decay of aligned state. These are spherical angles for the decay momentum in Fig. 1(b). In contrast, for description of three-body decays, we need three external correlations parameters. Euler angles  $\{\alpha, \beta, \gamma\}$  connected with three-body decay plane are convenient to use, see Fig. 1(c). The angle  $\alpha$  is analogous to the angle  $\varphi$  in two-body decay, and decay dynamics is independent from it for direct reactions we are interested in. The angle  $\beta$  describes an orientation of the decay plane relative  $\mathbf{q}$  and is analogous to the angle  $\theta$ , which describes the direction of decay in two-body case.

### III. THEORETICAL MODEL

The transition matrix element in Eq. (3) for the  ${}^1\text{H}({}^6\text{Li}, {}^6\text{Be})n$  reaction includes all interaction dynamics and is given in prior representation by

$$\begin{aligned} T_{fi} &= \langle \Psi_{M_{p_1}, M_{p_2}, M_n}^{(-)}(\mathbf{k}_x, \mathbf{k}_y, \mathbf{k}_f) | \\ &\quad \times \sum_i V_{pi} | \Psi_{M_A, \chi_{M_p}}(\mathbf{k}_i) \rangle, \\ \mathbf{k}_f &= \mu_f \left( \frac{\mathbf{k}'}{m_{123}} - \frac{\mathbf{k}_4}{m_4} \right), & \mu_f &= \frac{m_4 m_{123}}{m_4 + m_{123}}, \end{aligned} \quad (6)$$

where  $m_{123} = m_1 + m_2 + m_3$ ,  $\mathbf{k}_f$  is the relative momentum between c.m. of the  ${}^6\text{Be}$  nucleus and neutron,  $M_i$  denotes the spin projection of the  $i$ th particle,  $\Psi_{M_A}$  is the ground-state wave function of the  ${}^6\text{Li}$  nucleus,  $\chi_{M_p}(\mathbf{k}_i)$  is a plane wave describing relative motion of proton target and c.m. of the  ${}^6\text{Li}$  nucleus,  $\sum_i V_{pi}$  is composed of effective nucleon-nucleon interaction  $V_{pi}$  between proton target and projectile valence nucleons (marked as  $i$ ). Charge-exchange interaction with  $\alpha$  core should not lead to a population of the three-body continuum. The  $\Psi_{M_{p_1}, M_{p_2}, M_n}^{(-)}(\mathbf{k}_x, \mathbf{k}_y, \mathbf{k}_f)$  is the exact continuum wave function describing relative motion of the four final particles with ingoing-wave boundary conditions. To get  $\Psi^{(-)}$  one has to solve equations of the Faddeev-Yakubovsky type, taking into account the complex nature of the constituents. An exact solution has not been feasible up to now, and therefore approximate methods are required. We make approximations at the level of the reaction mechanism but the three-body structure of the involved nuclei is treated in a consistent way.

At low excitation energies of the  ${}^6\text{Be}$  nucleus, the relative velocities of the  ${}^6\text{Be}$  fragments are small and are restricted kinematically by the  $E_T$ . This means that interactions between these fragments have to be taken into account. But if collision is relatively fast and one-step processes are dominated, then a reasonable approximation for  $\Psi^{(-)}$  is the following factorization:

$$\begin{aligned} & \langle \Psi_{M_{p_1}, M_{p_2}, M_n}^{(-)}(\mathbf{k}_x, \mathbf{k}_y, \mathbf{k}_f) | \\ & \simeq \langle \chi_{M_n}^{(-)}(\mathbf{k}_f), \Psi_{M_{p_1}, M_{p_2}}^{(-)}(\mathbf{k}_x, \mathbf{k}_y) |, \end{aligned} \quad (7)$$

where  $\Psi_{M_{p_1}, M_{p_2}}^{(-)}(\mathbf{k}_x, \mathbf{k}_y)$  is a continuum three-body wave function of the  ${}^6\text{Be}$  system with excitation energy  $E_T$ .  $\chi_{M_n}^{(-)}(\mathbf{k}_f)$  is a distorted wave describing relative motion between c.m. of the  ${}^6\text{Be}$  and neutron, which depends on the respective relative coordinate between their center of mass.

If fragments are detected in coincidence, a number of various correlations can be obtained. The exclusive cross section

$$d^8\sigma/d\hat{\mathbf{k}}_f d\hat{\mathbf{k}}_x d\hat{\mathbf{k}}_y d\varepsilon dE_T,$$

contains the maximum possible information about the nuclear structure and reaction dynamics that can be extracted from a three-body breakup induced by the collision of two unpolarized nuclei (projectile and target). Exploration of this cross section is quite a challenge both experimentally (huge statistics is demanded) and theoretically, because it involves too many independent variables for transparent analysis. Integrating out some unobserved degrees of freedom brings us to less exclusive (increasingly inclusive) cross sections. Any integration over a dynamical variable, within its full range of variation, washes out the correlations defined by this degree of freedom. Cross sections after integration become less and less informative, but are simultaneously more suitable for theoretical modeling. On the other hand, often not all the particles produced by reaction are measured by detectors. Depending on the geometry of experimental installation and the efficiency of particle registration, some fragments avoid the measurements. Thus, for a proper comparison of theoretical calculations with experimental data, the integration over some

unobserved degrees of freedom should be done not within a full range of variation but taking into account response of the experimental setup. A practical way to perform this task is to use the Monte Carlo simulation of the reaction events. This allows us to make an additional simplification in theoretical treatment of the reaction dynamics, namely to substitute the distorted wave  $\chi_{M_n}^{(-)}(\mathbf{k}_f)$  by a plane wave. Then, the product of two plane waves in the transition matrix element (6) is reduced to the plane wave, which depends on the transferred momentum  $\mathbf{q}$

$$\chi_{M_n}^{(-)*}(\mathbf{k}_f) \chi_{M_p}(\mathbf{k}_i) \simeq \exp[-(\mathbf{q} \cdot \mathbf{R})] |1/2, M_p\rangle \langle 1/2, M_n|.$$

Finally, we treat the motion between c.m. of colliding systems within the plane-wave approximation (PWA) but the three-body decay dynamics is considered in a full complexity by taking into account all interactions between fragments. The disadvantage of such a treatment is that we can not calculate absolute contributions to cross sections from excitations with different values  $J^\pi$ . However, relative contributions from possible excitation modes leading to the excitation with the fixed value of  $J^\pi$  can be calculated. The absolute weights of different  $J^\pi$  excitations are restored by fitting to the experimental data. Hereby we remedy our simplified plane-wave treatment of the reaction dynamics.

The hyperspherical harmonics (HH) method is used for calculations of the three-body continuum wave function. The  $\alpha + p + p$  wave function (WF) of  ${}^6\text{Be}$  with outgoing asymptotics with fixed total momentum  $J$  and its projection  $M$  is obtained from solution of the Schrödinger equation with the source term

$$\begin{aligned} (\hat{H}_3 - E_T) \Psi_3^{JM(+)} &= \hat{O} \Psi_{\delta\text{Li}}^{J'M'}, \\ \hat{H}_3 &= \hat{T}_3 + V_{12}(\mathbf{r}_{12}) + V_{23}(\mathbf{r}_{23}) + V_{31}(\mathbf{r}_{31}). \end{aligned} \quad (8)$$

The wave function  $\Psi_3^{JM(+)}$  is linked with the wave function  $\Psi_{M_{p_1}, M_{p_2}}^{(-)}(\mathbf{k}_x, \mathbf{k}_y)$  in Eq. (7) by the reversal of time, which involves reversing the linear momenta ( $\mathbf{k}_x$  and  $\mathbf{k}_y$ ) and direction of the spin rotation ( $M_i \rightarrow -M_i$ ). The effective charge-exchange interaction between projectile and target nucleons with Gaussian form factor is used

$$\begin{aligned} \hat{V}(r) &= V_0 [c_{ivs} + c_{ivv}(\sigma^{(1)} \cdot \sigma^{(2)})] \\ &\times (\tau^{(1)} \cdot \tau^{(2)}) \exp[-r^2/r_0^2], \end{aligned} \quad (9)$$

where coefficients  $c_{ivs}$  and  $c_{ivv}$  define the strength of isovector-scalar and isovector-vector couplings. For such an interaction the transition operator in (8) is given in the PWA by an analytical expression

$$\begin{aligned} \hat{O} &\sim \sum_i f_i(q, r_i) [c_{ivs} + c_{ivv} \sigma_\mu^{(i)}] \tau_-^{(i)} Y_{lm}(\hat{\mathbf{r}}_i), \\ f_i(q, r_i) &= V_0 r_0^3 \sqrt{2} \pi^2 \exp[-(qr_0/2)^2] j_l(qr_i), \end{aligned} \quad (10)$$

where index  $i$  numbers the two valence nucleons. Such, relatively simple, choice allowed us to reproduce well the angular distributions of  ${}^6\text{Be}$  in Ref. [6].

The exclusive cross section of the direct reaction populating three-body continuum is, in general, an eightfold



differential. In our specific case, when an orientation of the reaction plane does not play a role, we work with a sevenfold differential cross sections and represent it by using the hyperspherical energy variables as follows:

$$\frac{d^7\sigma}{dq dE_T d\Omega_\kappa} = \sum_{SM_S} \sum_{JM,J'M'} \rho_{JM}^{J'M'}(q, E_T) A_{JMSM_S}^\dagger \times (E_T, \Omega_\kappa) A_{J'M'SM_S}(E_T, \Omega_\kappa), \quad (11)$$

where  $\rho_{JM}^{J'M'}$  is a density matrix and  $A_{JMSM_S}$  are three-body amplitudes depending on the  ${}^6\text{Be}$  excitation energy  $E_T$  and the five-dimensional hyperspherical solid angle

$$\Omega_\kappa = \{\theta_\kappa, \hat{\mathbf{k}}_x, \hat{\mathbf{k}}_y\}.$$

Variable  $\theta_\kappa$  is so-called hyperangle in the momentum space. It is related to energy distribution between Jacobi subsystems

$$E_x = E_T \sin^2(\theta_\kappa), \quad E_y = E_T \cos^2(\theta_\kappa).$$

In Eq. (11), the slow motion of fragments  $\alpha + p + p$  at low excitation energies is described by  $A_{JMSM_S}$  amplitudes and the state alignments are contained in the  $\rho_{JM}^{J'M'}$ .

Note the dependence of the density matrix  $\rho_{JM}^{J'M'}$  on the energy  $E_T$  and the absolute value of  $q$ . In general case there should be a dependence on  $\mathbf{q}$ , but the azimuthal angle of  $\mathbf{q}$  relative to the beam direction is defined by  $q$  and  $E_T$  for transfer reactions. Also note that the amplitudes  $A_{JMSM_S}$  explicitly depend on  $E_T$  and  $\Omega_\kappa$ , though it can be seen in Eq. (10) that there is also implicit dependence on  $q$ . The expression (11) is somewhat different from that stated in Ref. [9] as far as we explicitly provide summation over spin variables  $\{S, M_S\}$  of the three-body channel, which are not measurable (at least in foreseen realistic experimental scenarios).

#### IV. EXPERIMENT

The experiment was performed in the Flerov Laboratory of Nuclear Reaction, Joint Institute for Nuclear Research with the use of the ACCULINNA setup at U-400M cyclotron [6]. To carry out high-efficiency correlation measurements in the charge-exchange reaction  ${}^1\text{H}({}^6\text{Li}, {}^6\text{Be})n$ , maximal possible statistics of three-particle  $\alpha + p + p$  coincidences were desired. This condition required the detection of at least two particles by one of the telescopes (see Fig. 2) and the employment of a sophisticated experimental trigger and following data analysis.

The 47 AMeV  ${}^6\text{Li}$  beam was produced by the cyclotron U-400M and injected into ACCULINNA facility [10]. The beam energy was reduced to 35 AMeV using a carbon degrader and delivered to the well-shielded experimental room, located behind a 2 m thick concrete wall, where the background produced by cyclotron is considerably suppressed.

Experimental target and detectors setup were placed in stainless steel vacuum reaction chamber pumped out to a stationary pressure of  $\sim 10^{-6}$  mbar. The beam was focused on experimental target by means of lead collimator positioned between two ionization chambers, which compare the beam intensity before and after beam passage through the collimator. After the best setting of the ACCULINNA facility

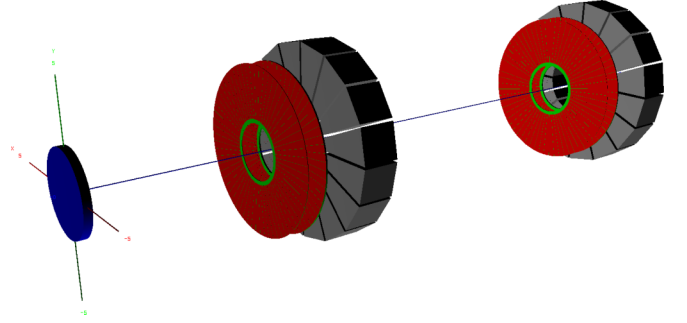


FIG. 2. Schematic view of the detector system employed for registration of the  ${}^1\text{H}({}^6\text{Li}, {}^6\text{Be})n$  reaction products. The origin of the left-handed laboratory frame is in the center of the hydrogen gas target (blue cylinder), each of two identical telescopes (T1 and T2) consists of two position-sensitive Si detectors (red) and the array of CsI(Tl) crystals (gray).

was found, the ionization chambers and the collimator were removed from the reaction chamber. The beam with intensity of about  $3 \times 10^7 \text{ s}^{-1}$  was focused to a  $\sim 3$  mm (FWHM) spot in the target plane and an energy spread better than 0.6% was achieved.

The detector array used for registration of the reaction products and a cryogenic hydrogen target are shown schematically in Fig. 2. The 4 mm thick target cell was equipped with 6  $\mu\text{m}$  stainless steel entrance and exit windows. For the sake of the heat shielding this cell was embedded in a protective volume supplied with 2  $\mu\text{m}$  windows of mylar coated with aluminum. The target geometry allowed us to detect reaction products emitted in downstream direction with full opening angle of  $90^\circ$ . The target cell was filled with hydrogen gas at a pressure of 3 bar and cooled down to 35 K. The difference between the pressure in target cell and the vacuum chamber caused the inflation of steel windows to lenticular form and resulting at maximal target thickness of 6 mm.

Reaction products were measured by two identical annular telescopes T1 and T2, see Fig. 2. Each telescope consisted of two position-sensitive silicon detectors and an array of 16 trapezoid CsI(Tl) crystals coupled with individual S8650 Si-photodiodes. The first double-sided silicon strip detector (DSSD), 300  $\mu\text{m}$  thick, had 32 sectors on the front side and 32 rings on the back side. The second layer was made of a single-sided silicon strip detector (SSSD) 1 mm thick, segmented into 16 sectors. The inner and outer diameters of the sensitive area of silicon detectors were 32 mm and 82 mm, respectively. The inner diameter of the silicon wafer was 28 mm. The assembly of CsI(Tl) crystals, 19 mm thick, had the inner and outer diameters of 37 mm and 97 mm, respectively. Dead layers of Si detectors were measured using  $\alpha$  source, those of CsI(Tl) detectors were estimated by MC simulations.

The overall thickness of each telescope was sufficient to stop all products of the investigated process with well-defined identification. DSSDs were intended to measure energy loss  $\Delta E$  of particles (with the threshold of  $\sim 300$  keV) and the positions of their hits. SSSD and CsI(Tl) detectors served for measurement of the remaining particle energy deposit.

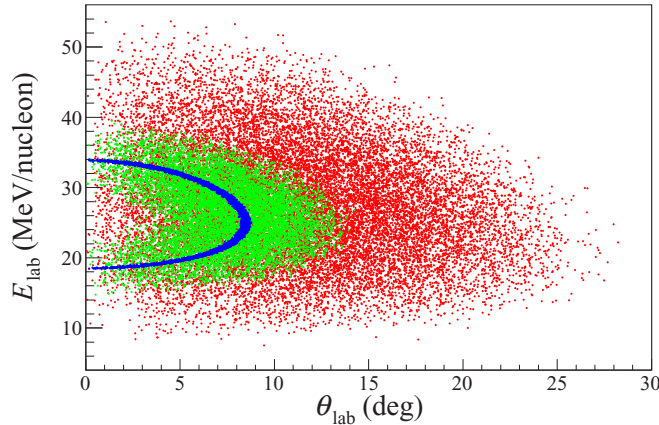


FIG. 3. Kinematic plot of the  ${}^1\text{H}({}^6\text{Li}, {}^6\text{Be})n$  reaction and  ${}^6\text{Be}$  decay obtained by MC simulation of the ground- and the first-excited-state population. The beam direction coincides with Z axis in laboratory frame.  $\theta_{\text{lab}}$  is the polar angle in laboratory frame,  $E_{\text{lab}}$  is the kinetic energy of the  ${}^6\text{Be}$  c.m. (blue dots) and its decay products ( $\alpha$  particles are shown by green dots and protons by red dots).

Moreover, signals from SSSD were branched to a fast time electronic circuit and used for formation of the trigger. The telescopes T1 and T2 were placed 91 mm and 300 mm downstream the target, respectively. Under an assumption that the reaction occurred in the center of the target, the T1 and T2 angular ranges in laboratory frame were  $9.9^\circ$ – $24.2^\circ$  and  $3.1^\circ$ – $7.8^\circ$ , respectively, see Fig. 3.

## V. DATA ANALYSIS

As a result of the experiment the  ${}^6\text{Be}$  energy spectra shown in Figs. 4(a) and 4(b) were obtained. The spectrum presented in Fig. 4(a) consists of two prominent peaks related to the population of the ground  $0^+$  and the first excited  $2^+$  states superimposed on the broad continuum. The width of the ground-state peak demonstrates overall instrumental resolution. This is a typical picture, which has been seen in a number of earlier observations (e.g., see Refs. [11–13]) where the low-energy  ${}^6\text{Be}$  spectrum was populated in charge-exchange reactions. Those results were based on the measurement of the missing mass spectra, and their treatment was often related to the analysis of the excitation spectrum and sometimes its angular behavior. The detection of three  ${}^6\text{Be}$  products  $\alpha + p + p$  provides complete kinematics measurement, and we can consider the population and the decay of the  ${}^6\text{Be}$  system in detail. Below we will focus on the parameters of the model related to the reaction mechanism and how they affect on the measured spectra formation.

The data analysis is performed by comparison of experimental data with Monte Carlo (MC) simulations based on the three-body decay model taking into account the population of the  $0^+$  and  $2^+$  states only, see Sec. III. Observables relevant to the  ${}^6\text{Be}$  decay will be treated in a specific  ${}^6\text{Be}$  center-of-mass frame with Z axis directed along the transferred momentum vector.

We have treated our data in the whole angular range of  $\theta_{\text{Be}}$  but we will make emphasis on the analysis of the

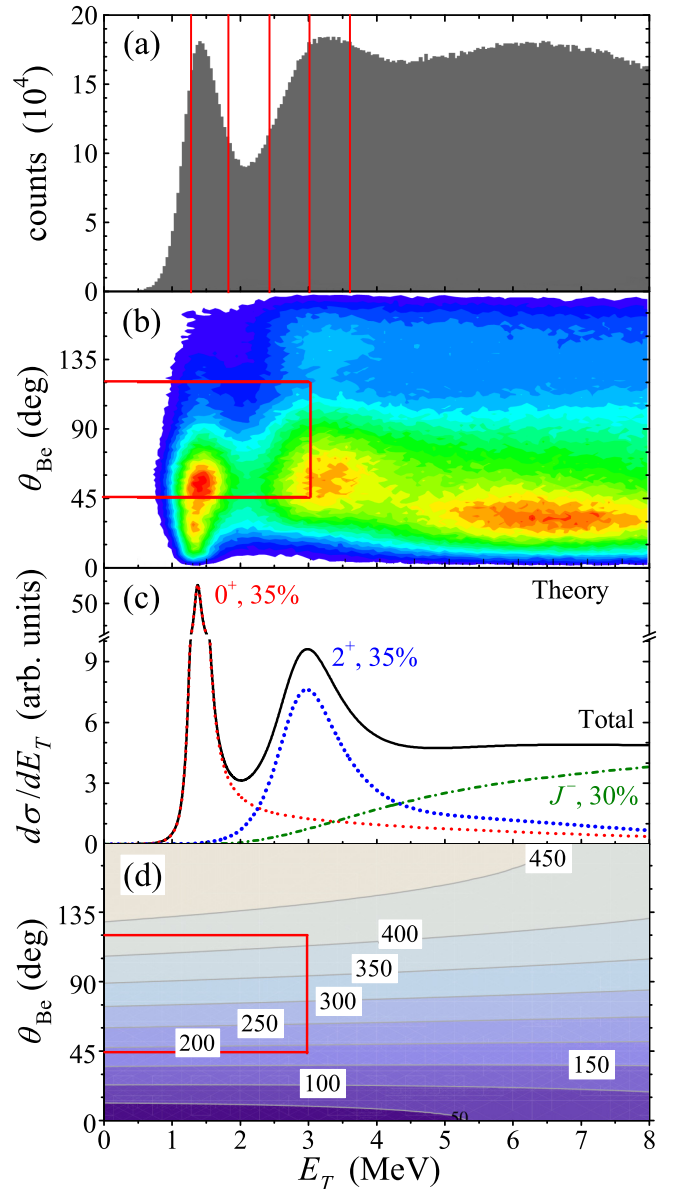


FIG. 4. Experimental data for  ${}^1\text{H}({}^6\text{Li}, {}^6\text{Be})n$  reaction. (a) shows the  ${}^6\text{Be}$  integral invariant mass spectrum measured in the whole range of  $\theta_{\text{Be}}$  angle. Red lines depict particular energy intervals to be treated (explanation is provided in text below). (b) shows the same data presented on the  $\{E_T, \theta_{\text{Be}}\}$  plane. (c) shows theoretical spectra with different  $J^\pi$  and their sum (black solid curve) fitting the data of (a) and (b). (d) shows contour plot of the transferred momentum (in MeV/c) on the  $\{E_T, \theta_{\text{Be}}\}$  plane. Red rectangle in (b) and (d) shows the region of interest for this work.

region of  $\theta_{\text{Be}} \in (45, 120)^\circ$  and  $E_T < 3.1$  MeV [see rectangle in Fig. 4(b)]. Both, the ground and first excited states, are well pronounced and are measured with sufficient statistics in this region. At smaller angles setup efficiency is severely suppressed by the telescope acceptance, while at larger angles population cross section is quite low. The model calculations were passed through a virtual measuring setup taking into account all major details of the experimental setup.

We will attempt to compare theoretical results with experimental data by fitting the three aspects of the density matrix related to investigated states:

- (i) Population ratio of the  $0^+$  ground state to the  $2^+$  first excited state;
- (ii) Intensity of the spin alignment for population of the  $2^+$  state;
- (iii) Interference phase between of the  $0^+$  and  $2^+$  states.

### A. Population rates for $0^+$ and $2^+$

Comparison of the simulated and experimental data in different angular intervals is given in Fig. 5. Experimental and simulated data are depicted by error bars and gray histograms, respectively. We can see that MC simulations have slightly better energy resolution than those of the experimental data. For that reason the simulated data were fitted to experimental ones by comparing the numbers of events corresponding to the population of ground state  $E_T < 2$  MeV and those forming the left slope of the  $2^+$  state peak  $2.5 < E_T < 3.1$  MeV.

In contrast with treatment of Ref. [6], here we do not include in the MC simulations the contribution of the  $J^-$  continuum (isovector soft dipole mode contribution). Instead, in the bottom panels of Fig. 5 we show results of the subtraction of simulated  $0^+$  and  $2^+$  contributions from the experimental spectrum. We can see that the IVSDM contributions are weakly dependent on the angular range. Another important thing we realize from this illustration is a significant contribution of the IVSDM for the right wing of the  $2^+$  resonance. This message is confirmed by theoretical calculations of Ref. [6], also shown in Fig. 4(c). We see that if we would like to study the  $0^+/2^+$  mixing only we should restrict our analysis mainly to the left wing of the  $2^+$  resonance with  $E_T < 3.1$  MeV.

### B. Spin-parity identification and density matrix parametrization

Before we turn to the charge-exchange reaction, some explanation how spin-parity identification based on density-matrix formalism was realized in our previous works is needed. The  $(t, p)$  reactions were used for population of three-body continuum states in  $^5\text{H}$  and  $^{10}\text{He}$  in Refs. [4,5,14]. Such two-neutron transfer reactions seem to be reliably described by dineutron transfer (two nucleons are transferred in a state with  $S = 0$ ). Then suppositions about Eq. (2) are fully valid and we get highly aligned density matrix in the transferred momentum frame with practically complete polar alignment

$$\rho_{JM}^{J'M'} \sim \delta_{M,\pm 1/2} \delta_{M',\pm 1/2} \quad \text{or} \quad \rho_{JM}^{J'M'} \sim \delta_{M,0} \delta_{M',0}, \quad (12)$$

for half-integer and integer spin of the initial system, respectively. Such strong alignment guarantee very expressed interference patterns for broad overlapping continuum states, which were used in the data analysis [4,5].

In general case the angular distribution of two-body decays is expressed in terms of associated Legendre polynomials  $P_L^M(x)$ . If a polar-aligned state with angular momentum  $L$  decays via emission of particle with  $J = 0$ , the angular distribution of the products may be expressed as

$$\frac{d\sigma}{d\cos\theta} \sim |P_L^0(\cos\theta)|^2, \quad (13)$$

for the selected alignment system, producing expressed and easy-to-interpret angular distribution.

In the case of the three-body decay, there exist an evident limit effectively reducing three-body motion to two-body motion:

$$\varepsilon \rightarrow 0. \quad (14)$$

The relative motion of one pair of particles (e.g., two protons) is fully suppressed and the three-body decay is determined

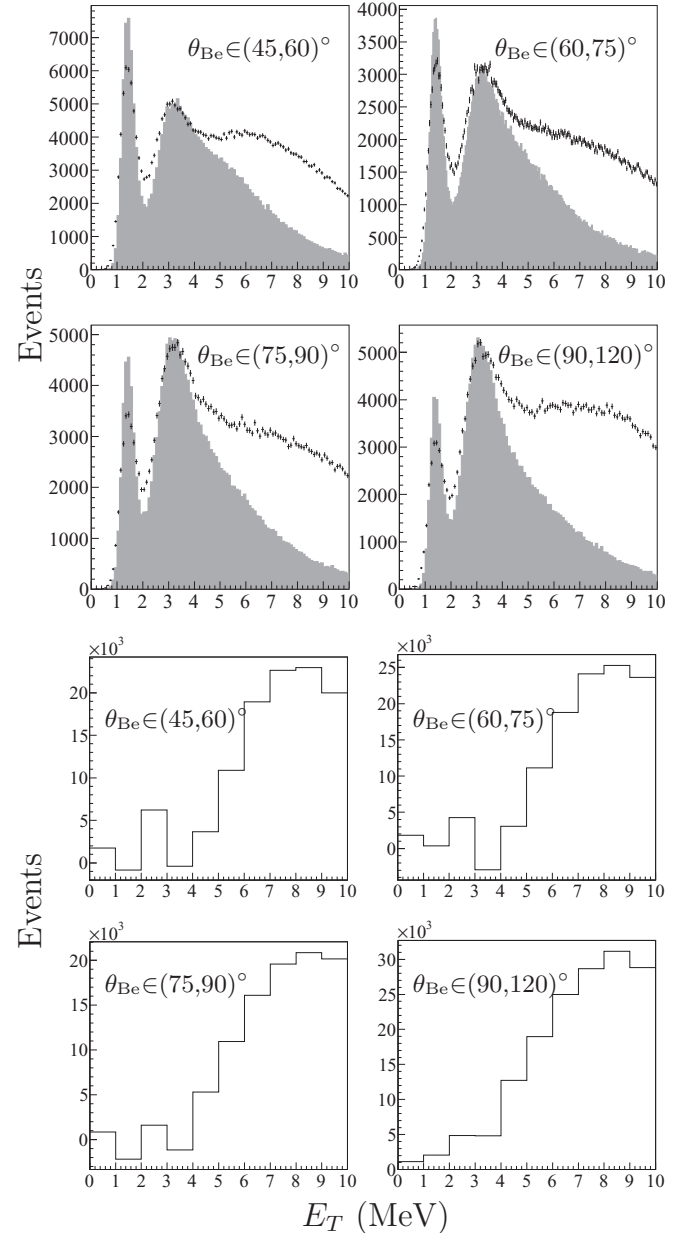


FIG. 5. Comparison experimental data and simulations including  $0^+$  and  $2^+$  states in different intervals of  $\theta_{\text{Be}}$ . In four top panels the experimental and simulated data are depicted by error bars and gray histogram, respectively. In four lower panels the subtraction of experimental and simulated histograms with energy bin of 1 MeV are shown for the same angular ranges. This subtraction shows the expected contributions of  $J^-$  states interpreted as isovector soft dipole mode contribution.

as two-body motion of  $\alpha$  particle and diproton with zero energy. In this limit we are getting for three-body decays the same very expressed angular distributions, but now in the corresponding  $\beta$  angle [see Fig. 1(c)].

We introduce the term quasibinary kinematic for three-body decay when the condition (14) is replaced by  $\varepsilon < x$  assuming a choice made for the upper limit of  $\varepsilon$  providing satisfactory accuracy for the studied process. For high-statistics measurements the value  $x$  can be gradually reduced to reveal expressed and easy-to-interpret correlation patterns.

In our analysis we fix some  $E_T$  and  $\theta_{\text{Be}}$  ranges and consider different correlation patterns within them. For internal correlations we consider  $\varepsilon$  and  $\theta_k$  distributions and for external correlations the most interesting are angular distributions  $\theta_\alpha$  of  $\alpha$  particles in the momentum transfer system,  $\theta_\alpha = \pi - \beta$ .

Density matrix, for population of the  $0^+$  and  $2^+$  states of  ${}^6\text{Be}$ , in the momentum transfer frame has relatively simple structure with the following nonzero terms:

$$\rho_{JM}^{J'M'} = \begin{pmatrix} \rho_{00}^{00} & & & & & \\ & \rho_{22}^{22} & & & & \\ & & \rho_{21}^{21} & & & \\ \rho_{00}^{20} & & & \rho_{20}^{20} & & \\ & & & & \rho_{2-1}^{2-1} & \\ & & & & & \rho_{2-2}^{2-2} \end{pmatrix}. \quad (15)$$

Formally, the terms of the density matrix  $\rho_{JM}^{J'M'}(q, E_T)$  for the pole reaction mechanism in Eq. (11) depend on two parameters:  $q$  and  $E_T$ . Looking in Fig. 4(d) it is easy to find that for energy and angular range of our interest momentum transfer depends only on angle, not on energy in a very good approximation. Thus it is reliable to consider the  $\rho_{JM}^{J'M'}$  dependence on  $E_T$  and  $\theta_{\text{Be}}$  in a factorized form. So, we presume that:

(i) The energy profile of the  $0^+$  and  $2^+$  states individually is defined by the energy dependence of the three-body amplitudes  $A_{JMSM_S}(E_T, \Omega_\alpha)$  as provided by three-body theoretical calculations.

(ii) The global population rate for the  $0^+$  and  $2^+$  states as fitted to experiment is defined by the parameter  $\rho_{00}^{00} / \sum_M \rho_{2M}^{2M}$ .

(iii) The following items are considered separately for each  $\{E_T, \theta_{\text{Be}}\}$  bin: the alignment for the  $2^+$  state ( $\rho_{2M}^{2M}$  dependence on  $M$ ) and the interference angle  $\varphi_{02}$  between  $0^+$  and  $2^+$  states, which define off-diagonal density matrix term parameterized as

$$\rho_{20}^{00} = \rho_{00}^{20} = \sqrt{\rho_{00}^{00} \rho_{20}^{20}} \cos(\varphi_{02}). \quad (16)$$

The expected alignment pattern for the  ${}^6\text{Be}$   $2^+$  state populated in the charge-exchange reaction induced by the potential Eq. (9) is illustrated in Fig. 6(a). Actually, more expressed alignment parametrizations were used for the MC simulations. Expressions

$$\rho_{2M} \sim \delta_{M0}, \quad (17)$$

$$\rho_{2M} \sim 1/5, \quad (18)$$

correspond to population of fully polar-aligned (17) and nonaligned (isotropic) (18)  $2^+$  state, respectively. If we consider the angular distribution of  $\alpha$ -particle fragment in the momentum transfer frame, then the isotropic density matrix

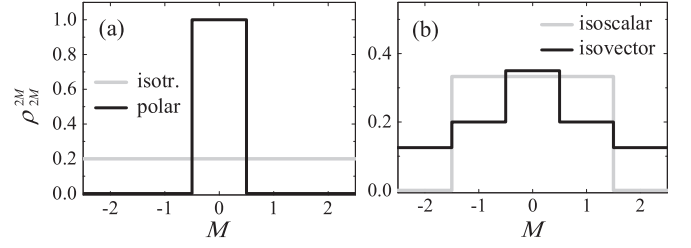


FIG. 6. The density matrix (15) spin structure for the  $2^+$  state. (a) Model approximations of isotropic and polar alignments actually used for MC simulations. (b) Isovector-scalar (constant  $c_{ivs}$ ) and isovector-vector (constant  $c_{ivv}$ ) couplings for potential (9).

should provide isotropic angular distribution for the isolated  $2^+$  state. Note that in the case of significant interference with other states an anisotropic distribution can be obtained even for isotropically populated state. With increase of the alignment more and more distinctive form of angular distribution should be obtained for the  $2^+$  state, tending to  $|P_2^0(\cos \theta_\alpha)|^2$  in the limit of polar alignment and under the condition (14).

Three extreme cases of interference between  $0^+ / 2^+$ , described by angle  $\varphi_{02}$ , are considered. We simulated the constructive interference ( $\varphi_{02} = 0^\circ$ ), destructive interference ( $\varphi_{02} = 180^\circ$ ) and situation when amplitudes of  $0^+$  and  $2^+$  states are summed incoherently ( $\varphi_{02} = 90^\circ$ ) for both cases determined by Eqs. (17) and (18). So, within this paper, six special cases are systematically illustrated, those given by two extreme cases of  $2^+$  alignment and three distinct cases of  $0^+ / 2^+$  interference, see, e.g., Fig. 7.

### C. Ground-state correlations

We start our analysis from the part of the  ${}^6\text{Be}$  excitation spectrum where the  $0^+$  ground state is only present. To eliminate the possible effects caused by the interference with the  $2^+$  state we restricted analysis here to excitation energy  $E_T \leq 1.4$  MeV, where contribution of the left wing of the first excited state can be reliably neglected [see Fig. 4(c)]. So, we have no free model parameters related to the reaction mechanism ( $0^+$  state by itself is isotropic by definition) there and internal correlations of  ${}^6\text{Be}$  decay products should be the same for the whole range of angle  $\theta_{\text{Be}}$ .

We can see in Fig. 7 that observed  $\varepsilon_T$  distributions are qualitatively different for different  $\theta_{\text{Be}}$  bins. The forms of theoretical distributions used as input for MC simulations are depicted by red lines. Events count presented on Y axis is related to simulated (gray histograms) and experimental data (crosses) only. Red line is drawn in different count range, which is not shown in figures. Theoretical input is introduced for illustration and convenience of comparison how are the observed forms affected by experimental setup. The main feature of theoretical input is that external correlations may vary with  $\theta_{\text{Be}}$  whereas internal ones (related to decay only) does not depend on reaction angle and their forms are the same for all panels of Fig. 7. In spite of this fact the simulated energy distributions (gray histograms) affected by virtual experimental setup are in a nice agreement with experimental data.



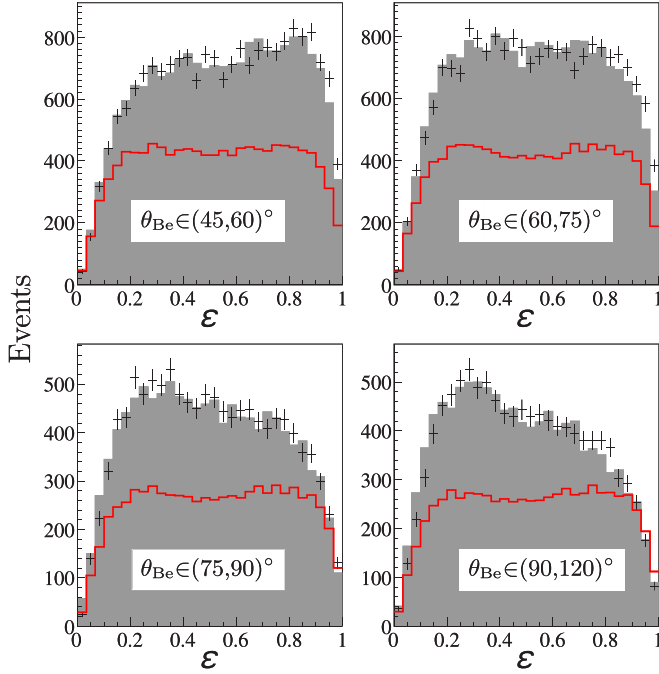


FIG. 7. Energy distributions  $\varepsilon_T$  for  ${}^6\text{Be}$  decay with  $E_T < 1.4$  MeV for different  $\theta_{\text{Be}}$  bins. Experimental and MC simulated data are depicted by crosses and gray histograms, respectively. Theoretical input (generated distributions used as input for MC simulations) is depicted by red line. Red line is depicted in different range to that used for experimental and simulated data (see Sec. VC for details).

The effect of the response of the experimental setup is much smaller for  $\varepsilon_Y$  distribution in the Y system and  $\cos\theta_k^{(T)}$  in the T system. It also very weakly depends on the kinematical range of  $\theta_{\text{Be}}$ . In Fig. 8 we show a typical picture of these distributions. Corrections induced by detection efficiency are noticeable, but not large.

Analysis of internal correlations for the ground state given here may be seen as a benchmark in two ways. On the one hand, it provides a confirmation of the theoretically predicted correlations, which were already tested against highly detailed experimental data of works [15,16]. Thus, the full consistency of our experiment with previous high-precision experiments [15,16] is demonstrated. On the other hand, the nice agreement in Figs. 7 and 8 means that the MC simulation is

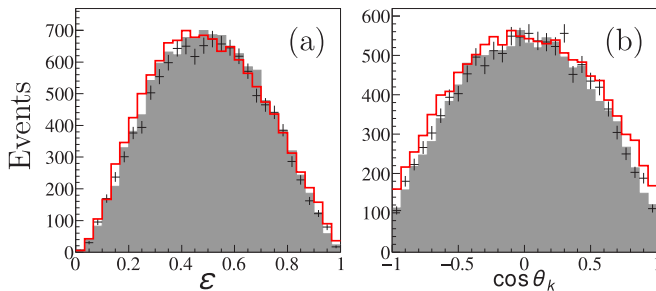


FIG. 8. (a) shows energy distributions  $\varepsilon_Y$  in the Jacobi Y system. (b) shows angular distribution  $\cos\theta_k^{(T)}$  in the Jacobi T system. Kinematical ranges are  $E_T < 1.4$  MeV and  $75^\circ < \theta_{\text{Be}} < 90^\circ$ .

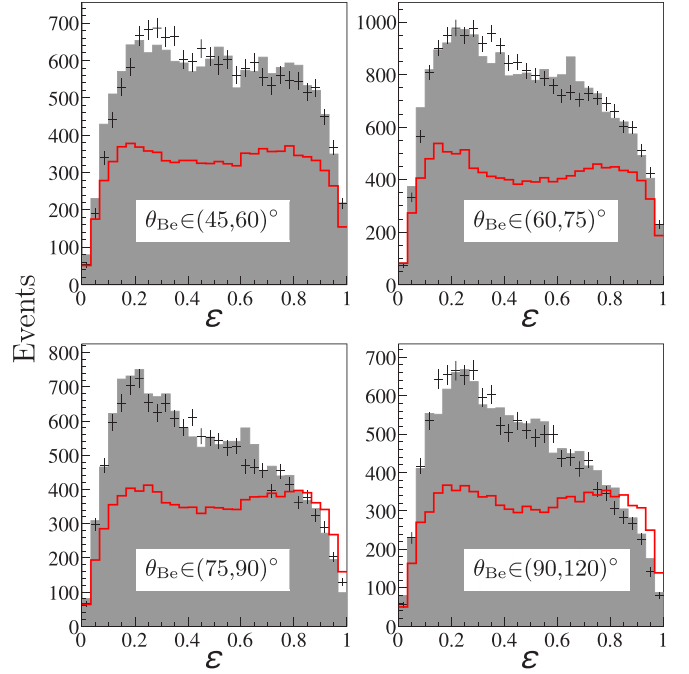


FIG. 9. Energy distribution  $\varepsilon_T$  for  ${}^6\text{Be}$  decay with  $1.4 < E_T < 1.9$  MeV (right slope of  $0^+$ ) for different  $\theta_{\text{Be}}$  bins. The simulation model settings are isotropic  $2^+$  state (NA) and no  $0^+/2^+$  interference ( $\varphi_{02} = 90^\circ$ ).

working reliably in the whole considered  $\theta_{\text{Be}}$  range and well represents the response of the experimental setup. This is an important prerequisite for the next more complicated steps of our analysis.

#### D. Correlations at the right slope of the $0^+$ state

Effects of  $0^+/2^+$  interference become important already on the right slope of the ground  $0^+$  state. Let us have a look at the energy range  $1.4 < E_T < 1.9$  MeV. If we look in theoretical predictions shown in Fig. 4(c), we can find that the relative probability of the  $2^+$  state population expected in this energy range is just around 1% of the  $0^+$  one. Nevertheless, it is sufficient to produce a significant modification in the correlations. This is the important motivation for use of correlations as a tool for studies: they are sensitive to amplitudes, not to probabilities. Therefore, the effects of even small-weight configurations can be drastically amplified.

First, we consider the evolution of energy  $\varepsilon_T$  distributions with angle  $\theta_{\text{Be}}$ . It is illustrated in Fig. 9 for the trivial case of isotropic and not interfering  $2^+$  state. The calculated distributions (red lines) are not much different from the ones shown in Fig. 7 and evidently do not depend on the angle  $\theta_{\text{Be}}$ . However, observable  $\varepsilon_T$  distributions are strongly sensitive to the angle  $\theta_{\text{Be}}$  and we can see that MC simulations are reliably taking the experimental efficiency into account in this range as well.

Much more fine effect of the alignment/interference on the energy distribution  $\varepsilon_T$  is illustrated in Fig. 10. We can see in this plot that there is weak dependence of the observed shape of the distribution on the alignment/interference settings. We recall that from the theoretical point of view there is no

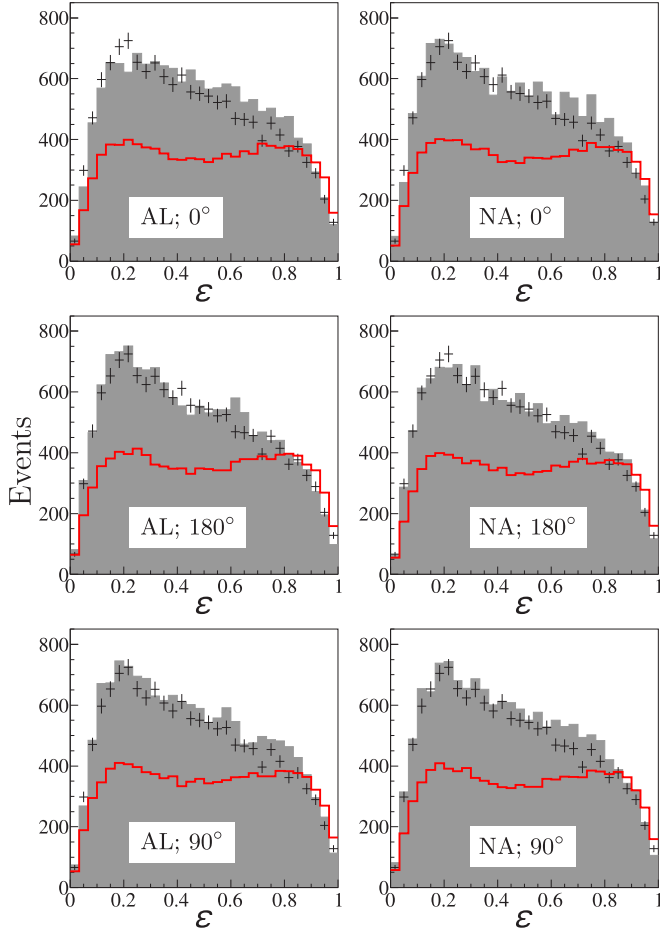


FIG. 10. Comparison of experimental energy distributions  $\varepsilon_T$  for  ${}^6\text{Be}$  decay with  $1.4 < E_T < 1.9$  MeV (right slope of  $0^+$ ) for  $75^\circ < \theta_{\text{Be}} < 90^\circ$  with different alignment/interference settings in theoretical model. The left column, compares data with theoretical model describing fully polar-aligned (AL)  $2^+$  state. The right column, corresponds to the isotropic (nonaligned, NA)  $2^+$  state. Top, middle, and bottom rows correspond to interference phase  $\varphi_{02}$  equal to  $0^\circ$ ,  $180^\circ$ , and  $90^\circ$ , respectively.

dependence of the  $\varepsilon_T$  distributions on the reaction mechanism. However, such a sensitivity of observable distributions arise in the experimental conditions, when isotropic efficiency for registration of decay fragments is not available. This effect has been already pointed out in Ref. [17] (see Fig. 6 of this work) for the  ${}^6\text{Be}$   $2^+$  data from experiment [16].

The dependence of Fig. 10 is quite curious, but too weak for practical application and deriving definite conclusions. To distinguish clearly the effects of alignment/interference it is better to consider external correlations in the momentum transfer frame. Angular distributions for  $\alpha$ -particle emission in the momentum transfer frame are illustrated in Fig. 11. We analyzed the  ${}^6\text{Be}$  decay in quasibinary approximation under the condition

$$\varepsilon_T < 0.2, \quad (19)$$

which ensured high enough statistics for the considered  $\{E_T, \theta_{\text{Be}}\}$  windows. It can be seen in Fig. 11 that already

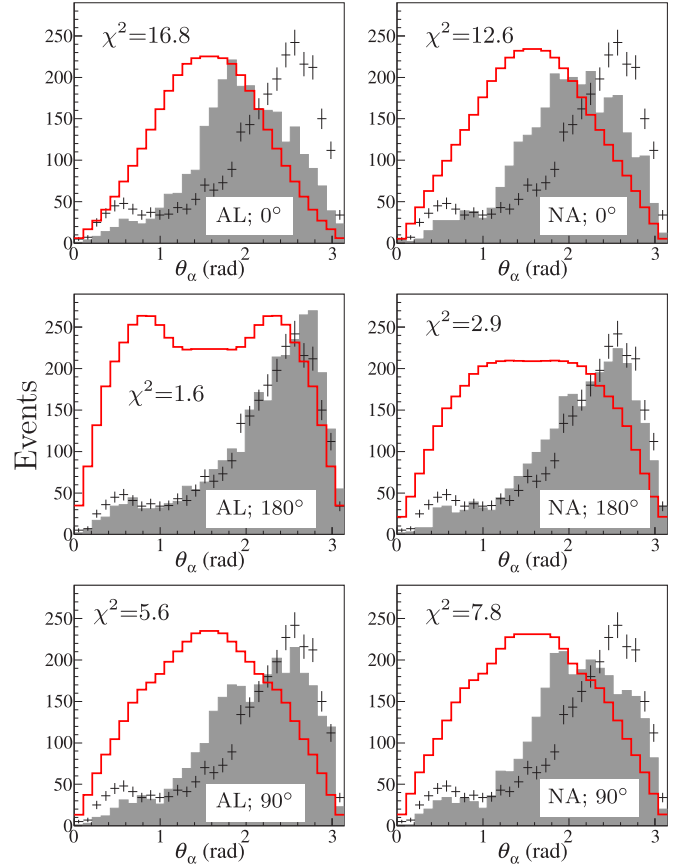


FIG. 11. Angular distributions for the  $\alpha$ -particle emission in the momentum transfer frame in the range  $1.4 < E_T < 1.9$  MeV and  $75^\circ < \theta_{\text{Be}} < 90^\circ$ . Alignment/interference settings are the same as in Fig. 10. Normalized  $\chi^2$  is indicated for comparison of experimental data with different theoretical model settings.

theoretical angular distributions are very sensitive to alignment/interference conditions. This sensitivity is further enhanced by imperfect experimental efficiency. It is clear that these distributions can be used to fix alignment/interference parameters with reasonable confidence. The analysis analogous to that of Fig. 11 was performed in the whole  $\theta_{\text{Be}}$  range and the results are summarized in Table I. Note, that such a strong sensitivity of the observed angular distributions is obtained just for  $\sim 1\%$  of the  $2^+$  state relative weight in the considered  $E_T$  energy window.

### E. Correlations at the left slope of the $2^+$ state

We may expect that effects of alignment/interference will be more pronounced in the region with higher probability of population of the  $2^+$  state. As illustration we provide here some details for the range  $2.5 < E_T < 3.1$  MeV. This corresponds to the left (rising) slope of the first excited  $2^+$  state of  ${}^6\text{Be}$ . It can be expected from Fig. 4(c)  $\sim 20\%$  of  $0^+$  contribution in this range making strong interference highly probable. Certain contamination of the correlations in this range by  $J^-$  contributions can be expected, but analysis shows that in reality it appears to be not of importance. Thus, the

TABLE I. The best fits to experimental data of density matrix parameters for different  $\{E_T, \theta_{Be}\}$  ranges. The fits were found using the figures with  $\theta_\alpha$  distribution for all six configurations of the theoretical model. Typical  $\chi^2$  values are not strongly different than those shown in Fig. 16 and all of them are equal or lower than 2.5.

$E_T$ (MeV)	$\theta_{Be} \in (45, 60)^\circ$	$\theta_{Be} \in (60, 75)^\circ$	$\theta_{Be} \in (75, 90)^\circ$	$\theta_{Be} \in (90, 120)^\circ$
1.4–1.9	AL; $\varphi_{02} = 135^\circ$	AL + 50% NA; $\varphi_{02} = 180^\circ$	AL; $\varphi_{02} = 180^\circ$	AL + 20% NA; $\varphi_{02} = 180^\circ$
1.9–2.5	NA + 10%AL; $\varphi_{02} = 135^\circ$	NA + 10% AL; $\varphi_{02} = 180^\circ$	NA; $\varphi_{02} = 180^\circ$	NA + 10%AL; $\varphi_{02} = 180^\circ$
2.5–3.1	NA + 10% AL; $\varphi_{02} = 180^\circ$	NA + 30% AL; $\varphi_{02} = 180^\circ$	NA + 20% AL; $\varphi_{02} = 180^\circ$	NA; $\varphi_{02} = 135^\circ$

analysis scheme here is quite stereotypical with that of the previous section.

Our first test is energy distribution  $\varepsilon_T$ , which gives minimal validation of the MC procedure quality, see Fig. 12. This energy distribution for the  $2^+$  state is qualitatively different from that for the  $0^+$  state. More fine effects of the alignment/interference on the observable distributions are illustrated for the selected  $\theta_{Be}$  range in Fig. 13.

All other distributions related to internal correlations,  $\theta_k$  in both Y and T systems and  $\varepsilon_Y$  show the same good agreement between experiment and theory. As a result of these studies we can declare two observations:

(i) The internal correlations do not seem to demonstrate noticeable dependence on the population conditions. This is a quite expected result for the narrow  $0^+$  state ( $\Gamma \approx 90$  keV), however, for much broader  $2^+$  state ( $\Gamma \sim 1$  MeV) this is not evident in advance. Thus, the internal motion of the three-body system seems to be really disentangled from the motion of the three-body system as a whole as it is presumed in the density matrix formalism.

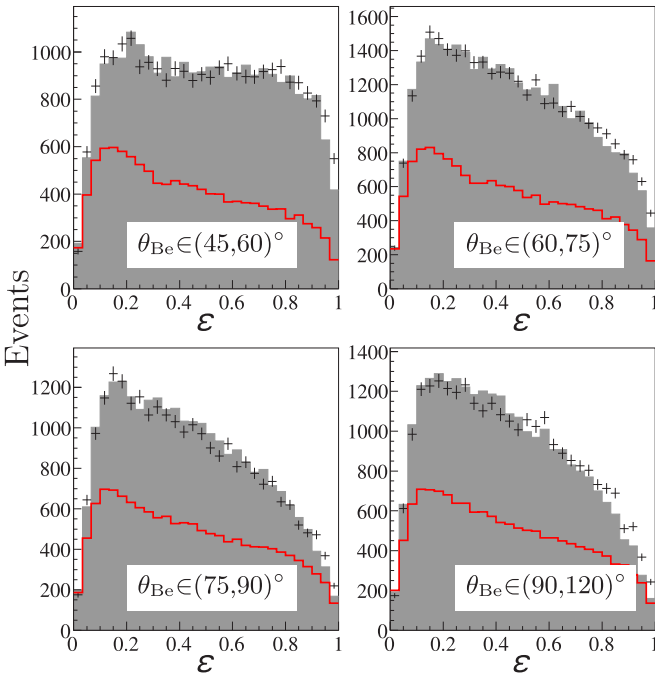


FIG. 12. Energy distribution  $\varepsilon_T$  for the  ${}^6\text{Be}$  decay with  $2.5 < E_T < 3.1$  MeV (left slope of  $2^+$ ) for different  $\theta_{Be}$  bins. The simulation model settings are isotropic  $2^+$  state (NA) and no  $0^+/2^+$  interference ( $\varphi_{02} = 90^\circ$ ).

(ii) The same theoretical input for the  $2^+$  state correlations was used for MC simulations in Ref. [16]. As far as the agreement between theory and experiment was also very good in this work, it means that there is a complete agreement between this experiment and the experiment [16]. The  ${}^6\text{Be}$  states were populated in a high-energy ( $E_{beam} \sim 70$  AMeV) knockout from  ${}^7\text{Be}$  beam in experiment [16]. This is very different reaction mechanism, so the internal correlations in the decay of relatively broad  $2^+$  state seem to be not sensitive also to this aspect of the reaction mechanism.

The analysis of external correlations is illustrated by Figs. 14 and 15 for two selected  $\theta_{Be}$  ranges. Again, the

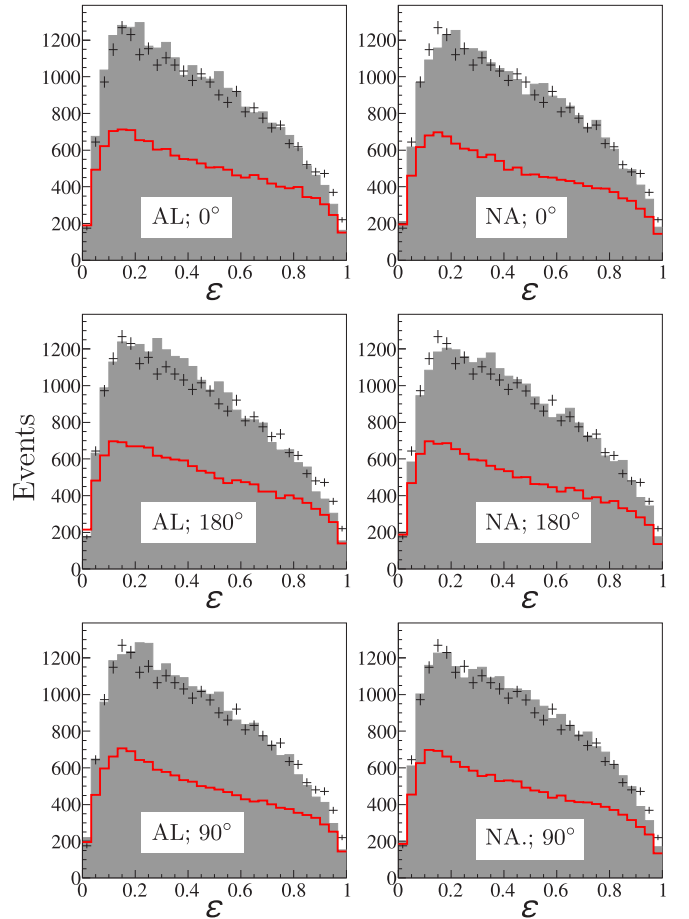


FIG. 13. Energy distribution  $\varepsilon_T$  for  ${}^6\text{Be}$  decay with  $2.5 < E_T < 3.1$  MeV (left slope of  $2^+$ ) for  $75^\circ < \theta_{Be} < 90^\circ$  and different alignment/interference settings, see also caption of the Fig. 10 for details.

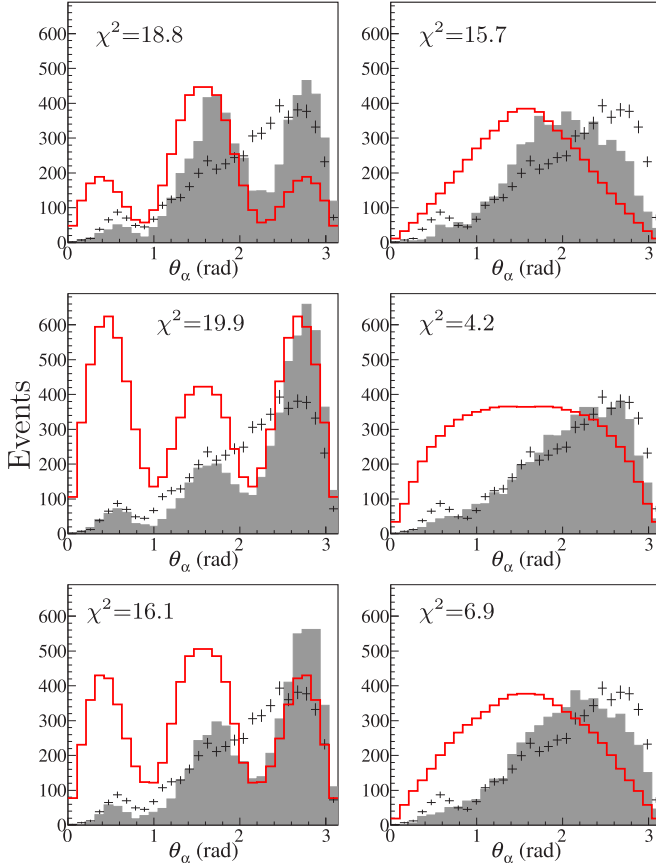


FIG. 14. Comparison of experimental and simulated angular distributions for the  $\alpha$ -particle emission in the momentum transfer frame in the range  $2.5 < E_T < 3.1$  MeV and  $75^\circ < \theta_{Be} < 90^\circ$ . Alignment/interference settings are the same as in Fig. 10.

sensitivity of the  $\theta_\alpha$  angular distributions to the alignment and interference conditions is very high (see  $\chi^2$  values in both figures) and, moreover, we can find the density matrix parameters for which near-perfect description of the distribution is provided. The results of our fits are summarized in the Table I and an example of best fits found for energy interval  $2.5 < E_T < 3.1$  MeV is shown together with obtained  $\chi^2$  values in Fig. 16. Part of the spectrum characterized by pure ground state ( $E_T < 1$  MeV) does not depend on the density-matrix parameters and it is not shown in the Table. We remark that typical values of  $\chi^2$  test are very similar to those shown in Fig. 16 and all of them are in the range  $0.9 < \chi^2 < 2.5$ .

#### F. Correlations at the right slope of the $2^+$ state

Let us consider now the energy range  $3.1 < E_T < 3.7$  MeV. It has been discussed above in the Sec. V A that important contribution IVSDM is expected here. Inclusive contribution of  $J^-$  states here can be theoretically evaluated as  $\sim 25\%$  from Fig. 4(c). We investigate how this fact is reflected in the correlations.

The typical picture of comparison of theoretical data with experimental ones for energy above the peak corresponding to the  $2^+$  state is shown in Fig. 17. It is obvious that experimental data cannot be fitted using  $0^+$  and  $2^+$  contributions only

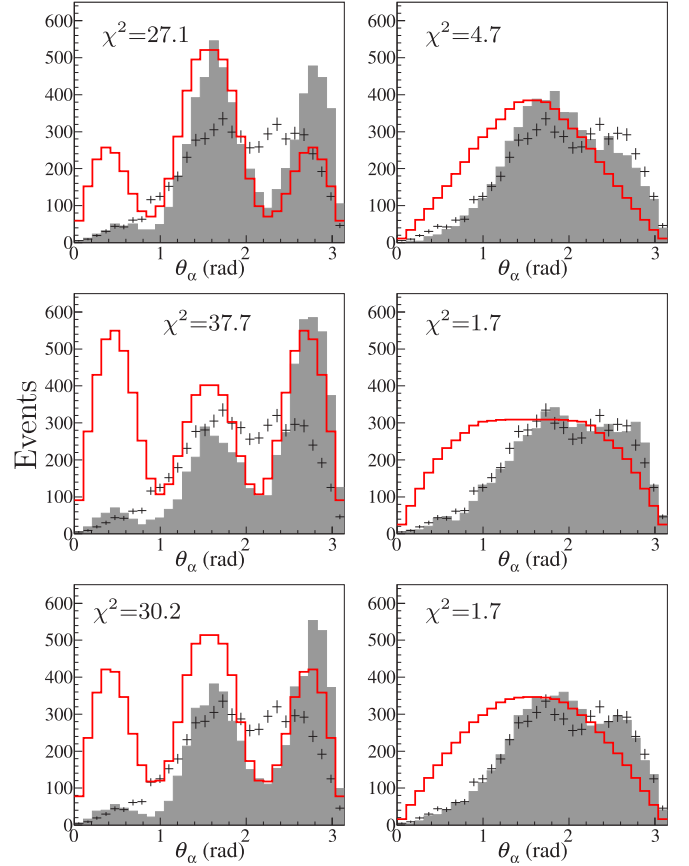


FIG. 15. Comparison of experimental and simulated angular distributions for the  $\alpha$ -particle emission in the momentum transfer frame in the range  $2.5 < E_T < 3.1$  MeV and  $90^\circ < \theta_{Be} < 120^\circ$ . Alignment/interference settings are the same as in Fig. 10.

because of the simulated events excess for all model interference/alignment settings at  $\theta_\alpha \rightarrow \pi/2$ . Moreover, it is clear that forward/backward asymmetry in the data is much higher than in the simulations. Such a forward/backward asymmetry is not possible for isolated states or for interference of states with the same parity. This means that asymmetry obtained from simulations based on the treated model can be related only to the response of the experimental setup. Simulations show that this effect is not sufficient to explain the observed forward/backward asymmetry. It means that additional interference of  $0^+$  and  $2^+$  with some  $J^-$  states is needed for explanation of the data. This can be seen as additional independent proof of the IVSDM contribution at  $E_T > 3$  MeV.

## VI. DISCUSSION

Studies of the three-body correlations for decays [18–20] or particle emission from states populated in reactions [3–5,21,22] are quite active in the recent years. In such studies the experimental question arises, which should be resolved to make theoretical interpretation possible: How much are the observed correlation patterns different from the actual? In this work we provide extensive illustration of this issue: even for the  ${}^6\text{Be}$  ground-state case, the observed three-body correlation patterns demonstrate strong variation depending



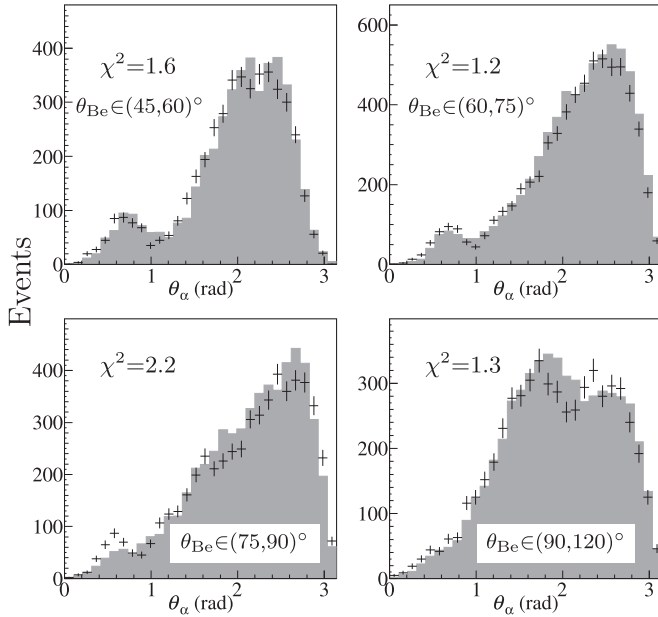


FIG. 16. Best fits of MC to experimental data obtained for energy interval  $2.5 < E_T < 3.1$  MeV. Notice that obtained normalized  $\chi^2$  values are than better those presented in Figs. 11, 14, and 15. See Table I for other treated energy interval.

on the specific region of the kinematical space. The influence of the experimental efficiency is especially harmful for studies of the external correlations. In this work we disentangle the effects related to response of the experimental setup from the effects of alignment/interference for energy range with overlapping  $0^+$  and  $2^+$  states of  ${}^6\text{Be}$ .

A general quantum-mechanical formal issue and important practical task of data interpretation is the extraction of the most complete quantum-mechanical information from the accessible observables. An important but very rare case when extraction of the complete quantum-mechanical information from data is possible is elastic scattering: from angular distributions one can, in principle, extract a set of phase shifts, which contains all possible information about this process. For other classes of experimental data extraction of complete quantum-mechanical information from observables suffers from different types of continuous and discrete ambiguities. For certain classes of reactions the most complete quantum-mechanical information that can be extracted is contained in the density matrix. Because of internal symmetries the density matrix could provide a very compact form of data representation depending just on very few parameters. In the case of the pole approximation considered for the  ${}^1\text{H}({}^6\text{Li}, {}^6\text{Be})n$  reaction there are just four parameters for specific kinematical point: the  $0^+/2^+$  ratio, the  $0^+/2^+$  relative phase, and two parameters describing  $2^+$  state alignment. The density-matrix approximation may be questioned for such complicated process as charge-exchange reaction. Despite this issue we demonstrate in this work principal ability to describe very complex and detailed multidimensional correlation patterns by applying this compact formalism.

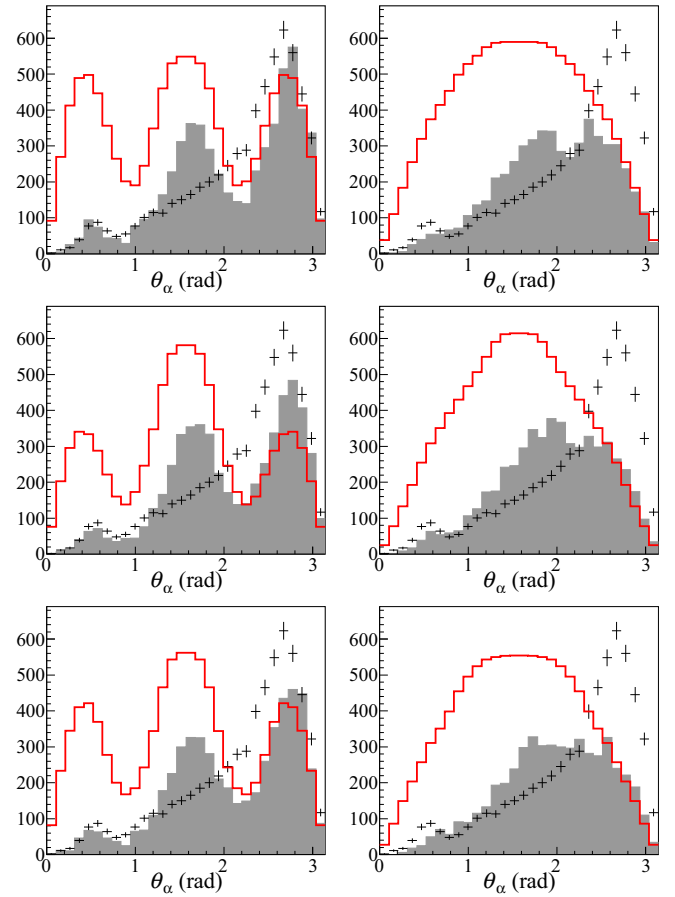


FIG. 17. Angular distribution of  $\alpha$  particles in the momentum transfer frame for the range  $3.1 < E_T < 3.7$  MeV and  $75^\circ < \theta_{\text{Be}} < 90^\circ$ . Alignment and interference conditions are the same as in Fig. 10.

In the mentioned recent three-body correlation studies, the detailed correlation data allowed us to resolve the following intriguing issues.

- (i) It was possible to check consistency of the long-range aspect of the three-body problem in continuum [19,21].
- (ii) We were able to figure out fine details of the decay dynamics for democratic decays by examples of  ${}^6\text{Be}$  and  ${}^{16}\text{Ne}$  ground and first excited states [15,21,22].
- (iii) Possibility to uncover weakly populated states due to interference with background states was demonstrated in Refs. [3,4].

In this work we add one more point to this list of scientific tasks, which can be resolved by correlation studies. The basic point here is that correlation data are very detailed to make possible investigation in different regions of the kinematical space. Such detailed information is not easily accessible in exotic dripline systems where secondary beams typically have low or modest intensities. Our work provides additional motivation for this type of reaction study.

## VII. CONCLUSIONS

The correlation data for three-body  $\alpha + p + p$  decay of the  ${}^6\text{Be}$  continuum with overlapping states populated in the  ${}^1\text{H}({}^6\text{Li}, {}^6\text{Be})n$  charge-exchange reaction were analyzed. The energy region  $E_T < 3$  MeV, where low-lying  $0^+$  and  $2^+$  states are populated, has been considered. Experimental data of high statistics ( $\sim 5 \times 10^6$  reconstructed events) allowed us to investigate correlations with reasonable resolution both in the  ${}^6\text{Be}$  excitation energy and in the reaction center-of-mass angle. Data analysis was carried out by using the comparison of experimental data with MC simulations taking into account the population of  $0^+$  and  $2^+$  states in the  ${}^6\text{Be}$  continuum and neglecting the population of  $J^-$  continuum. Our treatment showed that internal structure of three-body system with broad overlapping states may be revealed in correlations. While internal correlations are weakly sensitive to the investigated parameters (interference between the  $0^+$  and  $2^+$  states and alignment of  $2^+$  state), we observed strong sensitivity to those parameters in external correlations.

The principal opportunity to extract the density-matrix parameters, characterizing the reaction mechanism of population of the  ${}^6\text{Be}$  states, was demonstrated. The suggested

method of analysis allows for identification of such fine effects such as the ratio of the populated states, interference between them, and alignment of the states with  $J > 1/2$  for other nuclei, and it may be regarded as a general tool for similar tasks.

Nice examples of the employment of the three-body correlations for spin-parity identification are high-statistics experimental file  ${}^5\text{H}$  [3,4], low-statistics set  ${}^{10}\text{He}$  [5], and high-precision treatment of the three-body Coulomb continuum effects in  ${}^{16}\text{Ne}$  [21]. The results obtained in this work provide exemplary demonstration how the high-statistics few-body correlation data can be used for determination of the fine effects of the reaction mechanism. This work underline the importance of the high-statistics studies of the few-body correlations as important point of experimental agenda of RIB facilities.

## ACKNOWLEDGMENTS

This work was partly supported by Russian Science Foundation (Grant No. 17-12-01367) and Ministry of Education, Youth and Sports, Czech Republic (Projects No. LTT17003 and No. LM2015049).

- 
- [1] K. P. Artemov, V. Z. Goldberg, I. P. Petrov, V. P. Rudakov, and I. N. Serikov, *Yad. Fiz.* **14**, 1105 (1971) [*Sov. J. Nucl. Phys.* **14**, 615 (1972)], Study of  $\text{Li}^6$  Decay from Excited States.
- [2] M. S. Golovkov, L. V. Grigorenko, G. M. Ter-Akopian, A. S. Fomichev, Y. T. Oganessian, V. A. Gorshkov, S. A. Krupko, A. M. Rodin, S. I. Sidorchuk, R. S. Slepnev, S. V. Stepantsov, R. Wolski, D. Y. Pang, V. Chudoba, A. A. Korshennikov, E. A. Kuzmin, E. Y. Nikolskii, B. G. Novatskii, D. N. Stepanov, P. Roussel-Chomaz, W. Mittig, A. Ninane, F. Hanappe, L. Stuttgé, A. A. Yukhimchuk, V. V. Perevozchikov, Y. I. Vinogradov, S. K. Grishechkin, and S. V. Zlatoustovskiy, *Phys. Lett. B* **672**, 22 (2009).
- [3] M. S. Golovkov, L. V. Grigorenko, A. S. Fomichev, S. A. Krupko, Y. T. Oganessian, A. M. Rodin, S. I. Sidorchuk, R. S. Slepnev, S. V. Stepantsov, G. M. Ter-Akopian, R. Wolski, M. G. Itkis, A. A. Bogatchev, N. A. Kondratiev, E. M. Kozulin, A. A. Korshennikov, E. Y. Nikolskii, P. Roussel-Chomaz, W. Mittig, R. Palit, V. Bouchat, V. Kinnard, T. Materna, F. Hanappe, O. Dorvaux, L. Stuttgé, V. Lapoux, R. Raabe, L. Nalpas, A. A. Yukhimchuk, C. Angulo, V. V. Perevozchikov, Y. I. Vinogradov, S. K. Grishechkin, and S. V. Zlatoustovskiy, *Phys. Rev. Lett.* **93**, 262501 (2004).
- [4] M. S. Golovkov, L. V. Grigorenko, A. S. Fomichev, S. A. Krupko, Y. T. Oganessian, A. M. Rodin, S. I. Sidorchuk, R. S. Slepnev, S. V. Stepantsov, G. M. Ter-Akopian, R. Wolski, M. G. Itkis, A. S. Denikin, A. A. Bogatchev, N. A. Kondratiev, E. M. Kozulin, A. A. Korshennikov, E. Y. Nikolskii, P. Roussel-Chomaz, W. Mittig, R. Palit, V. Bouchat, V. Kinnard, T. Materna, F. Hanappe, O. Dorvaux, L. Stuttgé, C. Angulo, V. Lapoux, R. Raabe, L. Nalpas, A. A. Yukhimchuk, V. V. Perevozchikov, Y. I. Vinogradov, S. K. Grishechkin, and S. V. Zlatoustovskiy, *Phys. Rev. C* **72**, 064612 (2005).
- [5] S. I. Sidorchuk, A. A. Bezbakh, V. Chudoba, I. A. Egorova, A. S. Fomichev, M. S. Golovkov, A. V. Gorshkov, V. A. Gorshkov, L. V. Grigorenko, P. Jalůvková, G. Kaminski, S. A. Krupko, E. A. Kuzmin, E. Y. Nikolskii, Y. T. Oganessian, Y. L. Parfenova, P. G. Sharov, R. S. Slepnev, S. V. Stepantsov, G. M. Ter-Akopian, R. Wolski, A. A. Yukhimchuk, S. V. Filchagin, A. A. Kiryashkin, I. P. Maksimkin, and O. P. Vikhlyantsev, *Phys. Rev. Lett.* **108**, 202502 (2012).
- [6] A. Fomichev, V. Chudoba, I. Egorova, S. Ershov, M. Golovkov, A. Gorshkov, V. Gorshkov, L. Grigorenko, G. Kaminski, S. Krupko, I. Mukha, Y. Parfenova, S. Sidorchuk, R. Slepnev, L. Standlyo, S. Stepantsov, G. Ter-Akopian, R. Wolski, and M. Zhukov, *Phys. Lett. B* **708**, 6 (2012).
- [7] S. Treiman and C. Yang, *Phys. Rev. Lett.* **8**, 140 (1962).
- [8] I. Shapiro, V. Kolybasov, and G. Augst, *Nucl. Phys.* **61**, 353 (1965).
- [9] L. V. Grigorenko, I. A. Egorova, R. J. Charity, and M. V. Zhukov, *Phys. Rev. C* **86**, 061602 (2012).
- [10] A. M. Rodin, S. I. Sidorchuk, S. V. Stepantsov, G. M. Ter-Akopian, A. S. Fomichev, R. Wolski, V. B. Galinskiy, G. N. Ivanov, I. B. Ivanova, V. A. Gorshkov, A. Y. Lavrentev, and Y. T. Oganessian, *Nucl. Instrum. Methods Phys. Res., Sect. A* **391**, 228 (1997).
- [11] D. Tilley, C. Cheves, J. Godwin, G. Hale, H. Hofmann, J. Kelley, C. Sheu, and H. Weller, *Nucl. Phys. A* **708**, 3 (2002).
- [12] X. Yang, L. Wang, J. Rapaport, C. D. Goodman, C. C. Foster, Y. Wang, E. Sugarbaker, D. Marchlenski, S. de Lucia, B. Luther, L. Rybarczyk, T. N. Taddeucci, and B. I. Park, *Phys. Rev. C* **52**, 2535 (1995).
- [13] V. Guimaraes, R. Kuramoto, R. Lichtenhaler, G. Amadio, E. Benjamin, P. de Faria, A. Lepine-Szily, G. Lima, J. Kolata, G. Rogachev, F. Becchetti, T. O'Donnell, Y. Chen, J. Hinnefeld, and J. Lipton, *Nucl. Phys. A* **722**, C341 (2003).
- [14] M. S. Golovkov, L. V. Grigorenko, A. S. Fomichev, Y. T. Oganessian, Y. I. Orlov, A. M. Rodin, S. I. Sidorchuk, R. S. Slepnev, S. V. Stepantsov, G. M. Ter-Akopian, and R. Wolski, *Phys. Lett. B* **588**, 163 (2004).

- [15] L. V. Grigorenko, T. D. Wisner, K. Mercurio, R. J. Charity, R. Shane, L. G. Sobotka, J. M. Elson, A. H. Wuosmaa, A. Banu, M. McCleskey, L. Trache, R. E. Tribble, and M. V. Zhukov, *Phys. Rev. C* **80**, 034602 (2009).
- [16] I. A. Egorova, R. J. Charity, L. V. Grigorenko, Z. Chajecski, D. Coupland, J. M. Elson, T. K. Ghosh, M. E. Howard, H. Iwasaki, M. Kilburn, J. Lee, W. G. Lynch, J. Manfredi, S. T. Marley, A. Sanetullaev, R. Shane, D. V. Shetty, L. G. Sobotka, M. B. Tsang, J. Winkelbauer, A. H. Wuosmaa, M. Youngs, and M. V. Zhukov, *Phys. Rev. Lett.* **109**, 202502 (2012).
- [17] L. V. Grigorenko, I. G. Mukha, and M. V. Zhukov, *Phys. Rev. Lett.* **111**, 042501 (2013).
- [18] K. Miernik, W. Dominik, Z. Janas, M. Pfützner, L. Grigorenko, C. R. Bingham, H. Czyrkowski, M. Cwiok, I. G. Darby, R. Dabrowski, T. Ginter, R. Grzywacz, M. Karny, A. Korgul, W. Kusmierz, S. N. Liddick, M. Rajabali, K. Rykaczewski, and A. Stolz, *Phys. Rev. Lett.* **99**, 192501 (2007).
- [19] L. V. Grigorenko, T. D. Wisner, K. Miernik, R. J. Charity, M. Pfützner, A. Banu, C. R. Bingham, M. Cwiok, I. G. Darby, W. Dominik, J. M. Elson, T. Ginter, R. Grzywacz, Z. Janas, M. Karny, A. Korgul, S. N. Liddick, K. Mercurio, M. Rajabali, K. Rykaczewski, R. Shane, L. G. Sobotka, A. Stolz, L. Trache, R. E. Tribble, A. H. Wuosmaa, and M. V. Zhukov, *Phys. Lett. B* **677**, 30 (2009).
- [20] P. Ascher, L. Audirac, N. Adimi, B. Blank, C. Borcea, B. A. Brown, I. Companis, F. Delalee, C. E. Demonchy, F. de Oliveira Santos, J. Giovinazzo, S. Grévy, L. V. Grigorenko, T. Kurtukian-Nieto, S. Leblanc, J.-L. Pedroza, L. Perrot, J. Pibernat, L. Serani, P. C. Srivastava, and J.-C. Thomas, *Phys. Rev. Lett.* **107**, 102502 (2011).
- [21] K. W. Brown, R. J. Charity, L. G. Sobotka, Z. Chajecski, L. V. Grigorenko, I. A. Egorova, Y. L. Parfenova, M. V. Zhukov, S. Bedoor, W. W. Buhro, J. M. Elson, W. G. Lynch, J. Manfredi, D. G. McNeel, W. Reviol, R. Shane, R. H. Showalter, M. B. Tsang, J. R. Winkelbauer, and A. H. Wuosmaa, *Phys. Rev. Lett.* **113**, 232501 (2014).
- [22] K. W. Brown, R. J. Charity, L. G. Sobotka, L. V. Grigorenko, T. A. Golubkova, S. Bedoor, W. W. Buhro, Z. Chajecski, J. M. Elson, W. G. Lynch, J. Manfredi, D. G. McNeel, W. Reviol, R. Shane, R. H. Showalter, M. B. Tsang, J. R. Winkelbauer, and A. H. Wuosmaa, *Phys. Rev. C* **92**, 034329 (2015).